

Ultrasound-Responsive Nanodelivery System of GPC3-Targeting and Sonosensitizer for Visualized Hepatocellular Carcinoma Therapy

Juying Zhang¹, Xia Luo¹, Xin Yang¹, Hanmei Li¹, Qiong Jiang¹, You Yang¹, Menglin Luo¹, Zijun Ma¹, Ping He¹, Linli Feng¹, Ling Li¹, Maochun Zhang¹, Yang Li^{2,3}, Jinhong Yu^{1,3}

¹Department of Ultrasound, Affiliated Hospital of North Sichuan Medical College, Innovation Centre for Science and Technology of North Sichuan Medical College, Nanchong, Sichuan, 637000, People's Republic of China; ²Department of Radiology, Affiliated Hospital of North Sichuan Medical College, Nanchong, Sichuan, 637000, People's Republic of China; ³Department of Ultrasound, Yuechi People's Hospital, Guangan, Sichuan, 638300, People's Republic of China

Correspondence: Jinhong Yu, Email yujinhong@nsmc.edu.cn

Purpose: The incidence of hepatocellular carcinoma (HCC) is continuously increasing, and the mortality rate remains high. Thus, more effective strategies are needed to improve the treatment of HCC.

Methods: In this study, we report the use of a visualized glypican-3 (GPC3)-targeting nanodelivery system (named GC-NBs) in combination with sonodynamic therapy (SDT) to enhance the therapeutic efficacy for treating HCC. The obtained nanodelivery system could actively target hepatocellular carcinoma cells and achieve ultrasound imaging through phase changes into nanobubbles under low-intensity ultrasound irradiation. Meanwhile, the released chlorine e6 (Ce6) after the nanobubbles collapse could lead to the generation of reactive oxygen species (ROS) under ultrasound irradiation to induce SDT.

Results: Both in vitro and in vivo experiments have shown that GC-NBs can accumulate in tumour areas and achieve sonodynamic antitumour therapy under the navigation action of glypican-3-antibody (GPC3-Ab). Furthermore, in vitro and in vivo experiments did not show significant biological toxicity of the nanodelivery system. Moreover, GC-NBs can be imaged with ultrasound, providing personalized treatment monitoring.

Conclusion: GC-NBs enable a visualized antitumour strategy from a targeted sonodynamic perspective by combining tumour-specific targeting and stimuli-responsive controlled release into a single system.

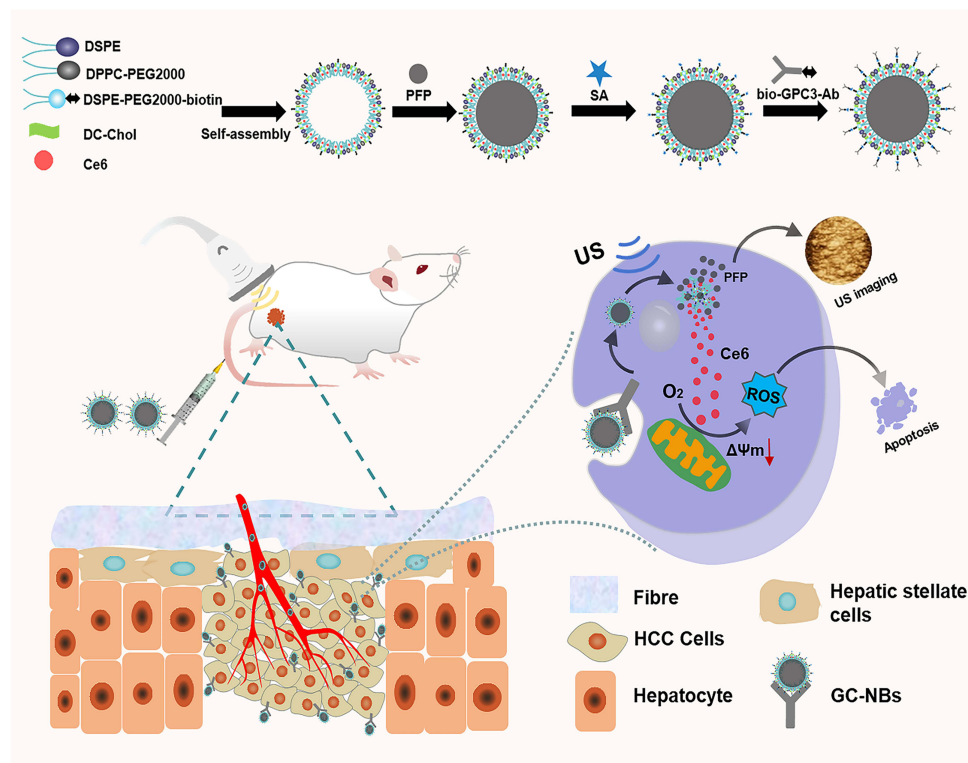
Keywords: Glypican-3, nanodelivery system, ultrasound imaging, sonodynamic therapy, hepatocellular carcinoma

Introduction

Hepatocellular carcinoma (HCC) is one of the most common malignancies and a leading cause of cancer-related mortality worldwide.¹ The global incidence of HCC ranks sixth among malignant tumours, and its mortality rate ranks third. The similarity between incidence and mortality underlines the dismal prognosis associated with this disease.^{2,3} In recent years, to cure HCC, many strategies, such as liver resection, liver transplantation, chemoembolization, transarterial embolization and biological therapy, have been widely employed.⁴⁻⁶ However, the survival of HCC patients remains low due to the limitations of current strategies. Therefore, novel and effective therapeutic methods for HCC are urgently needed.

Sonodynamic therapy (SDT), which involves the activation of sonosensitizers under low-intensity ultrasound irradiation to induce cytotoxicity and cause oxidative damage of tumor cells through intracellular generate reactive oxygen species (ROS) generated by thermal effects and non-thermal cavitation, is attracting increasing interest in the noninvasive treatment of tumours.⁷⁻¹¹ On the basis of the known fundamental mechanisms of cell apoptosis or necrosis induced by SDT, such as DNA, lipids, and proteins damages, sonosensitizers are considered pivotal elements used for maximum effectiveness.^{12,13} As an innovative and effective photosensitizer and sonosensitizer, Ce6 produces higher

Graphical Abstract



levels of singlet oxygen under ultrasound irradiation and has better antitumour effects; however, their clinical applications are limited by poor water solubility and delivery efficiency.^{14,15} As self-assembled, closed spherical delivery systems, liposomal vehicles are biocompatible, biodegradable, nontoxic and nonimmunogenic and are both hydrophilic and hydrophobic by nature. Liposome-incorporated pharmaceuticals are protected from the inactivating effect of external conditions but do not cause undesirable side reactions.¹⁶ Therefore, liposomal encapsulation of Ce6 is highly desirable for improving its water solubility.

To improve the delivery efficiency (DE) of nanoparticles to solid tumours, ligand-conjugated nanoparticle-based targeted SDT has been proposed.¹⁷ Glypican-3 (GPC3) is a heparan sulfate proteoglycan that functions as a Wnt coreceptor and is one of the key regulators of HCC tumour progression. Furthermore, GPC3 is an oncofoetal proteoglycan anchored to the cell membrane and is overexpressed in 70% of HCC tumours but not in healthy adult liver tissue; thus, it can be used as an ideal target for therapy.^{18–20} Therefore, the use of GPC3-Ab as the targeted ligand of the nanodelivery system was intended to provide precise targeting and resulted in the aggregation of nanoparticles at HCC tumour sites.

To ensure better therapeutic effects, in addition to effectively aggregating in the tumour area of nanodelivery systems, these drugs must also be able to be released into the tumour site. Meanwhile, ultrasound imaging could be used to monitor efficiency and to guide therapeutic administration during the therapeutic process, improving the efficiency and accuracy of SDT. It has been reported that perfluoropentane (PFP) has an outstanding ability to transform from the liquid phase to the gas phase under ultrasound irradiation, termed acoustic droplet vaporization (ADV), which can be effectively applied to ultrasonic imaging and cause stable cavitation.^{21–23} Contrast-enhanced ultrasound (CEUS) is a new diagnostic and therapeutic technique that utilizes the backscattered echo enhancement of microbubble ultrasound contrast agents (UCAs) in the circulatory system to improve tissue resolution.²⁴ Thus, PFP was loaded inside liposomes, and ADV and ultrasound-targeted microbubble destruction (UTMD) were induced by low-intensity ultrasound to achieve controlled drug release and *in vitro* imaging.^{25,26} Importantly, stable cavitations, which exert biophysical effects through

the oscillation of NBs, have been proven to enhance local drug penetration by forming artificial pores in cell membranes.^{27,28} In addition, ultrasonic cavitation triggered the reassembly of liposomes to decorticate the protein corona and reinitiate active ligand/receptor-mediated transcytosis to achieve more effective tumour accumulation.²⁹

In this work, we designed and fabricated a novel nanodelivery system, GC-NBs, with a GPC3-Ab-targeted sonodynamic function for the visualization of hepatocellular carcinoma. With this nanodelivery system, GC-NBs can actively target tumour cells through GPC3-Ab and accumulate in the tumour area. Under low-intensity ultrasound irradiation, PFP-mediated liquid–gas phase transition enhanced ultrasound imaging; simultaneously, Ce6 was released after the collapse of the nanobubbles, thereby producing excess reactive oxygen species (ROS) and promoting tumour cell/tissue apoptosis with ultrasound assistance, realizing targeted sonodynamic antitumour therapy. This study provides a promising and attractive strategy for the treatment of hepatocellular carcinoma.

Material and Methods

Materials

1,2-dipalmitoyl-sn-glycerol-3-phospho-lipid ethanolamine-polyethylene glycol-2000 (DPPE-mPEG2000) and 1,3-diphenylisobenzofuran (DPBF) were purchased from Aladdin Biochemical Technology Co., Ltd. (Shanghai, China). 1,2-dipalmitoyl-sn-glycerol-3-phosphatidylcholine (DPPC) and 2,7-dichlorofluorescein diacetate (DCFH-DA) were purchased from Aldrich Chemical Co. (St. Louis, MO, USA). DSPE-PEG2000-biotin, chlorine e6 (Ce6) and DC-Chol were purchased from Shanghai Macklin Biochemical Technology Co., Ltd. (Shanghai, China). Perfluoropentane (PFP, boiling point 29 °C) was obtained from Shanghai Acme Biochemical Co., Ltd. (Shanghai, China). Biotin labeling kit was obtained from Friendbio Science & Technology Co., Ltd. (Wuhan, China). Streptavidin (SA), FITC-labelled goat anti-rabbit IgG, GPC3-Ab and EDTA were obtained from Boster Biological Technology Co., Ltd. (Wuhan, China). Calcein-AM/PI and CCK-8 assays were purchased from Beyotime Biotechnology Co., Ltd. (Shanghai, China). DMEM, RPMI 1640, penicillin/streptomycin and FBS were purchased from Gibco (Thermo Fisher, USA). 4',6-diamidino-2-phenylindole (DAPI) was purchased from Solarbio Science & Technology Co., Ltd. (Beijing, China). Annexin V-FITC/PI was obtained from Jiangsu KeyGEN Bio TECH Corp., Ltd. (Nanjing, China).

Synthesis of GC-NBs

The GC-NBs were synthesized by a lipid thin film and a simple facile acoustic-emulsification method.³⁰ In brief, DPPC, DPPE-mPEG2000, DSPE-PEG2000-biotin, DC-Chol, and Ce6 were mixed with absolute ethanol at a mass ratio of 5:1:1:0.5:0.3 and then transferred to a rotary evaporator under vacuum at 40 °C for 1 h to form a homogeneous dark lipid film. Subsequently, 3 mL of PBS was added to the bottle of the lipid mixture for hydration. Homogeneous liposomes were obtained by ultrasound in an ice bath. Then, 1 mL of the above liposome solution was sonicated in an ice bath with the power set at 100 W for a total of 180 seconds after mixing with 100 µL of PFP. To purify the nanoparticles, they were centrifuged (8000 rpm, 3 min) and washed with PBS, in which the lower layer of brown liquid was the biotin-Ce6-NBs. The centrifugation and washing steps were repeated three times. The Ce6-NBs were obtained by replacing DSPE-PEG2000-biotin with DPPE-mPEG2000. Biotin-Ce6-NBs were incubated at room temperature with 50 µg of SA for 20 min. Free SA was removed by washing with PBS by centrifugation for 3 min at 8000 rpm, followed by 20 min of incubation at 4 °C with 20 µL of biotin-GPC3-Ab to allow the formation of GPC3-Ce6-NBs (designated GC-NBs). Free ligands were removed by washing with PBS under the same centrifugation conditions. All the experimental steps were performed in the dark.

Morphological Characterization of GC-NBs

After the GC-NBs were diluted (GC-NBs:PBS=1:10), the particle size distribution and zeta potential were measured by dynamic light scattering analysis. The newly prepared GC-NBs were stored in PBS at 4 °C for 5 days. The particle size and Polydispersity index (PDI) of the GC-NBs were measured to study their stability. The morphology and size of the liposomes were measured by transmission electron microscopy (TEM).

Determination of Ce6 Loading and Interactions Between GPC3-Ab and Ce6-NBs

The loading status of Ce6 in the GC-NBs was analysed by ultraviolet–visible spectrometer. Moreover, Ce6 loading and the conjugation of GPC3-Ab to Ce6-NBs were detected by immunofluorescence assay. In particular, GC-NBs were incubated with FITC-labelled goat anti-rabbit IgG (2 mg/mL) at 4 °C for 20 min in the dark and washed with PBS three times (8000 rpm, 3 min). FITC-IgG-GC-NBs were obtained. All the experiments were carried out in triplicate.

The Ce6 Encapsulation Efficiency (EE) of GC-NBs

The content of loaded Ce6 was determined by ultraviolet–visible spectrometer. Freshly prepared solutions of Ce6 at concentrations of 1.25 µg/mL, 2.5 µg/mL, 5 µg/mL, 10 µg/mL, 20 µg/mL, and 40 µg/mL were used to construct standard curves. Next, the supernatant containing free Ce6 was collected after centrifugation for 3 min at 8000 rpm, and Ce6 concentrations were determined on UV–visible spectrometer. The amounts of noncombined Ce6 were obtained. Ce6 EE (%) = (Input Ce6 quality - Quality of Ce6 in supernatant)/Input Ce6 quality × 100%.

In vitro responsive drug release from GC-NBs activated by ultrasound

For measuring the drug-releasing patterns, the GC-NBs were collected and incubated in a conical flask with 20 mL of PBS (100–120 rpm/min) at 37 °C. The GC-NBs were separated into the following 3 groups: pH 7.4, pH 5.5, pH 5.5+US, ultrasound (1 MHz, 2 W/cm², 50% duty cycle) was applied for the active drug release. At pre-determined time intervals, a 2 mL release medium was taken out for measurement. The same amount of fresh buffer was then added to maintain the sink condition. The Ce6 concentrations were determined by UV-vis spectrometry and the amounts of cumulative release were calculated.

Single Oxygen Production

In vitro ultrasound-triggered singlet oxygen generation was measured by 1,3-diphenylisobenzofuran (DPBF). DPBF (20 µmol/L) was mixed with PBS, Ce6, Ce6-NBs, or GC-NBs, and its absorption at 415 nm was monitored every 2 minutes during ultrasound irradiation at a power intensity of 1 MHz, 2 W/cm² with 50% duty cycle. The remaining DPBF was calculated as follows: (initial mixture absorption value - absorption value after US)/initial mixture absorption value × 100%.

In vitro Ultrasound Imaging

The GC-NBs were placed in the thermostat water bath at 37 °C, which was filled with deionized water. Subsequently, the GC-NBs were exposed to ultrasound irradiation (1 MHz, 2 W/cm², 50% duty cycle) for 1 min, 2 min, 3 min, 4 min or 5 min. Two dimensional (2D) and CEUS mode imaging signals were observed and collected in real time by ultrasound diagnostic system. The corresponding echo intensity of the above ultrasound images was analysed by ImageJ software.

Cell Cultures and Animals

The HepG2 cells were purchased from Sichuan Bio Biotechnology Co.,Ltd. The HepG2 cell was cultured in high-glucose Dulbecco's modified Eagle's medium (DMEM), and the H22 cell was cultured in RPMI 1640 medium, both supplemented with 10% FBS and 1% penicillin/streptomycin, at 37 °C under 5% CO₂. Exponentially growing cells were used in all experiments.

Female BALB/c normal mice (6–8 weeks, 18–20 g) were purchased from the Animal Center, North Sichuan Medical College. All animal experiments were approved by the Animal Research Committee of North Sichuan Medical College and performed following the Guide for the Use and Care of Laboratory Animals.

Cell Targeting Efficiency and Flow Cytometry

The ability of GC-NBs to target HepG2 cells was characterized using fluorescence microscopy. HepG2 cells were seeded in confocal dishes at a density of 2×10⁴ cells per dish, grown for 24 h, and divided into the following two groups: Ce6-NBs and FITC-IgG-GC-NBs. The cells were incubated for an additional 6 h after different treatments containing the

same Ce6 concentration. Then, the cells were fixed with 4% paraformaldehyde, and the nuclei were stained with DAPI for 5 min. The cells were washed with PBS for observation under a fluorescence microscope (Olympus). In addition, the cellular uptake of GC-NBs was quantitatively analysed by flow cytometry. Excitations: 550 nm for Ce6 and emissions: 670 nm for Ce6.

Hemolysis Assay

Blood samples were centrifuged, and red blood cells were extracted and diluted with normal saline. Subsequently, blood samples were mixed with normal saline, deionized water (positive control), or GC-NBs at various concentrations (0, 0.5, 1.0, 2.0, 4.0, 8.0 $\mu\text{g/mL}$, $n = 3$). The samples were collected after incubation at 37 °C for 1 h. The supernatants were collected, and the absorbance was measured by ultraviolet–visible spectrometer at 545 nm to determine the hemolysis ratios.

In vitro Cytotoxicity and SDT Capability

The cells were plated into a 96-well plate (1×10^4 cells/well) at 24 h confluence. After attaching to the bottom of the wells, the GC-NBs were diluted with DMEM at various concentrations of Ce6 (0, 0.5, 1.0, 2.0, 4.0, and 8.0 $\mu\text{g/mL}$, $n = 3$). After 24 h of incubation, HepG2 cell and human umbilical vein endothelial cell (HUVEC) viability was assessed by cell counting kit 8 (CCK–8) assay. According to the manufacturer’s protocol, 10 μL of CCK–8 solution was added to each well, and the plates were incubated for 30 min at 37 °C in the dark. The absorbance at 450 nm was read in a microplate reader, and the cell viability was calculated as the A450 of treated cells/A450 of control cells $\times 100\%$.

HepG2 cells were seeded into 24-well plates at a density of 4×10^4 cells per well overnight. The cells were separated into the following 5 groups: control, Ce6-NBs, GC-NBs, Ce6-NBs+US, and GC-NBs+US. An ultrasound probe was coated with couplant and tightly attached to the bottom of the 24-well plates (1 MHz, 2 W/cm², 50% duty cycle, 60s/well) after 8 h of incubation with different drugs for the group requiring sonication. Then, the cells were washed with PBS and stained with Calcein-AM/PI. A fluorescence microscope was used to image the stained cells. The corresponding fluorescence intensity was measured by ImageJ software.

Apoptosis Assays

To investigate apoptosis induced by the GC-NBs, HepG2 cells (3×10^5 cells/mL) were plated in 6-well plates overnight adhesion. The cells were separated into the following 5 groups: control, Ce6-NBs, GC-NBs, Ce6-NBs+US, and GC-NBs+US. Thereafter, the adherent cells were incubated with various formulations for 12 h. Selected cells (US groups) were additionally irradiated by ultrasound (1 MHz, 2 W/cm², 50% duty cycle, 60s/well). After 8 h of incubation, the HepG2 cells were collected by ethylenediaminetetraacetic acid (EDTA), centrifuged and washed with PBS. Subsequently, the collected cells were stained with 5 μL of Annexin V-FITC and 5 μL of propidium iodide (PI) for 15 min in the absence of light and analysed via flow cytometry.

In vitro ROS Generation

Intracellular ROS generation after different treatments in HepG2 cells was examined by a 2,2-dichlorofluorescein diacetate (DCFH-DA) fluorescent probe. Briefly, HepG2 cells were incubated in a 24-well plate at a density of 4×10^4 per well for 24 h. The cells were separated into the following 5 groups: Control, Ce6-NBs, Ce6-NBs+US, GC-NBs, and GC-NBs+US. After 8 h of treatment with different drugs, the cells were irradiated with US (1 MHz, 2 W/cm², 50% duty cycle, 60 s/well). Then, all groups were changed to a mixture of DMEM and DCFH-DA at a volume ratio of 1:1000 and incubated for an additional 30 min at 37 °C. After three washes with PBS, a fluorescence microscope (excitation wavelength, 488 nm; emission wavelength, 525 nm) was used to confirm the reactive oxygen species production, and the corresponding fluorescence intensity was measured by ImageJ software.

Mitochondrial Membrane Potential Assay

The JC-1 probe was used to analyse the mitochondrial membrane potential ($\Delta\Psi\text{m}$) during the early stage of tumour cell apoptosis via fluorescence microscopic imaging. HepG2 cells were seeded into 12-well plates at a density of 8×10^4 cells/well overnight and were separated into the following 5 groups: control, Ce6-NBs, GC-NBs, Ce6-NBs+US, and GC-NBs+US.

After different treatments, the HepG2 cells were stained with a JC-1 probe at 37 °C for 20 min in the dark and then washed twice with JC-1 staining buffer before detection. The average fluorescence intensity was determined by ImageJ software.

In vivo Targeting Capability and Biodistribution

According to existing studies confirming the high and close expression of GPC3 in HepG2 human cells and H22 murine cells, BALB/c mice were inoculated with H22 cancer cells ($1 \times 10^7/\text{mL}$) at the subcutaneous right buttocks to establish a mouse tumour-bearing model.³¹ When the tumour size reached 100 mm^3 , the tumour-bearing mice were randomly divided into two groups ($n = 3$ per group): the Ce6-NBs group and the GC-NBs group. Fluorescence imaging of the tumour and main tissues was further performed using Ce6 for fluorescence labelling to observe its targeting capability and biodistribution in vivo at 1 h, 3 h, 6 h, 9 h and 24 h after drug injection.

GC-NBs Enhance Retention at Tumour Sites

Tumour-bearing mice were randomly divided into two groups ($n = 3$ per group): the Ce6-NBs group and the GC-NBs group. Ce6-NBs and GC-NBs were injected intravenously into mice, the mice were sacrificed after 48 hours, the tumours were collected, and the mice were fixed with 4% (w/v) paraformaldehyde. DAPI was added to locate the tumour tissue, the fluorescence intensity of Ce6 in the tissue was observed via fluorescence microscopy, and the fluorescence intensity was quantitatively analysed via ImageJ software.

In vivo Targeted SDT and Safety Evaluation

Tumour-bearing mice established as described above were randomly divided into the control (injection of normal saline), Ce6-NBs, GC-NBs, Ce6-NBs+US and GC-NBs+US groups ($n=3$ per group). On days 10, 12, 14, 16, 18, 20, and 22, the mice were intravenously administered with drugs at the 5 mg/kg dose of Ce6. The Ce6-NBs+US and GC-NBs+US groups were irradiated with ultrasound (2 W/cm^2 , 2 min) three hours after intravenous injection for each treatment. Tumour length (L) and width (W) were measured with callipers every treatment, and the tumour volume ($V, \text{ mm}^3$) was calculated. The body weight of each group was monitored every treatment as an indicator of systemic toxicity. After the mice were sacrificed after the therapeutic experiments, we measured the tumour weight of each group, generated a tumour growth curve, and calculated the tumour inhibition rate. The tumour volume inhibition rate was calculated as $(1 - \text{experimental group tumour volume}/\text{control group tumour volume}) \times 100\%$, and the tumour mass inhibition rate was calculated as $(1 - \text{mass of the tumour in the experimental group}/\text{mass of the tumour in the control group}) \times 100\%$. The tumours were kept in 4% (w/v) paraformaldehyde overnight for HE staining, TUNEL assays and Ki-67 staining. In addition, blood was collected from the mice via the eyeball blood collection method, and blood biochemical analysis was performed. The major organs (heart, liver, spleen, lungs, and kidneys) were weighed and collected for HE staining.

In vivo Ultrasound Imaging

To characterize the US imaging performance of the GC-NBs, tumour-bearing mice were treated with a GC-NBs emulsion (200 μL) followed by US irradiation. US images were captured and analysed using an US imaging system in 2D mode and CEUS mode. Quantitative data were analysed by mapping the region of interest and comparing the echo intensity obtained after GC-NBs administration with that recorded prior to administration.

Statistical Analysis

All data are presented as the mean \pm standard deviation (SD), and statistical analysis of the data was performed by Student's *t*-test and one-way ANOVA. Statistical significance level was set as $p < 0.05$.

Results and Discussion

Synthesis and Characterization of GC-NBs

The GC-NBs were prepared by a lipid thin film and a simple facile acoustic-emulsification method. As shown in Figure 1A, the shell membrane consisted of DPPC, DPPE-mPEG2000, DSPE-PEG2000-biotin, DC-Chol, and Ce6.

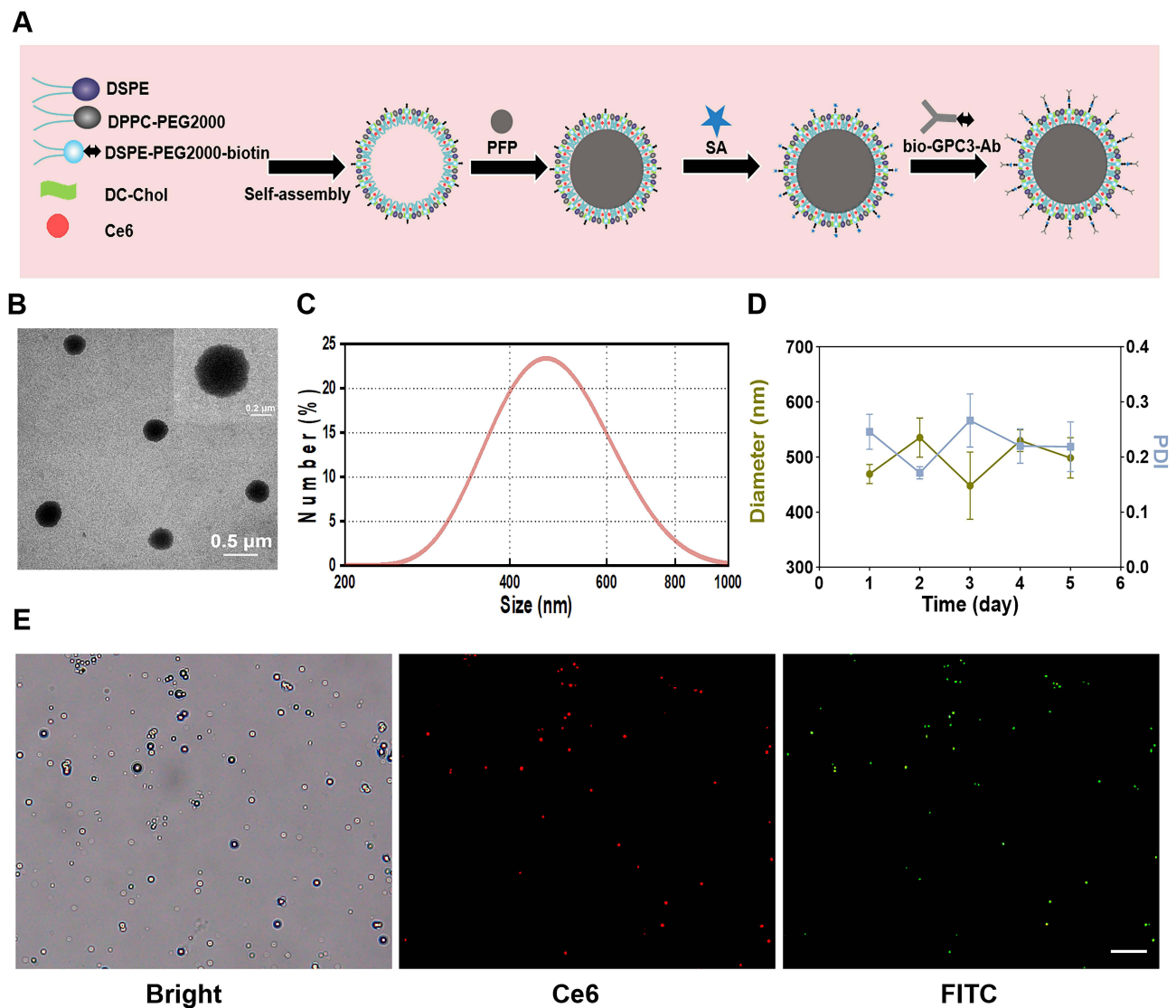


Figure 1 Characterization of GC-NBs.

Notes: (A) Structure of GC-NBs. (B) GC-NBs were observed by TEM. (C) Size distribution of GC-NBs. (D) The change of hydrated particle size and PDI of GC-NBs. (E) Observation of GC-NBs in a white light channel, red light channel and green channel under a confocal microscope. Scale bar: 5 μ m.

A study showed the relationship between shell hardness and the encapsulation efficiency of a drug nanodelivery system. As in our study, adding cholesterol to lipids was helpful for improving the stability and membrane hardening effect of the nanodelivery system.^{32,33} Then, Ce6-NBs were filled with PFP and connected to GPC3-Ab by the “avidin–biotin” bridge. Under confocal microscopy and TEM, the GC-NBs were spherical with a smooth surface and were dispersed and uniform (Figure 1B). Dynamic light scattering (DLS) measurements revealed that the average diameter of the GC-NBs was approximately 489.4 ± 24.7 nm (Figure 1C). As a solid tumor, HCC provides a unique tumor microenvironment, with features such as a lack of vascular tissue support, the frequent formation of porous channels between tumor vascular endothelial cells, and a vascular endothelial space of approximately 1μ m.³⁴ Additionally, It has been reported that nanocarriers with particle sizes between 380 nm and 780 nm can be passively targeted to tumour sites through large interendothelial gaps.³⁵ Therefore, the GC-NBs with a particle size of approximately 500 nm prepared in the current study are theoretically sufficient to pass through the vascular endothelial space of HCC by EPR. The size of the GC-NBs was greater according to DLS than according to TEM. This difference may be due to the freeze-drying process used for TEM imaging of the sample. In addition, the DLS method measures the hydrodynamic diameter. The hydrodynamic

diameter consists of the core and all molecules attached to the nanoparticle surface, such as ions and water molecules. Therefore, the hydrodynamic diameters obtained using the DLS method are larger than those determined by microscopy.^{36,37} The zeta potential measured by a Malvern Zeta Sizer was -17.5 mV for the GC-NBs (Figure S1). A negative zeta potential is conducive to the prevention of nanodelivery system self-aggregation and protein aggregation with negative potential *in vivo*.³⁸ GC-NBs were placed in PBS at 4 °C, and there were no statistically significant differences in the particle size distribution or PDI on day 5 compared with day 1, indicating that the GC-NBs had a high level of stability (Figure 1D). These features established the ground for subsequent applications.

It has been reported that antibodies or peptides can be attached to the surface of nanobubbles.³⁹ Chen et al synthesized DOX-loaded lipid NBs by conjugating PD-L1 mAb to the shells of NBs via streptavidin-biotin interactions.⁴⁰ In this study, GC-NBs were synthesized by conjugating GPC3-Ab onto the surface of Ce6-NBs through streptavidin-biotin bridge, and we utilized this proven approach to achieve the combination of targeting and SDT. The conjugation of GPC3-Ab with Ce6-NBs was confirmed by an immunofluorescence assay. FITC-labelled goat anti-rabbit IgG was added to the GC-NBs, which were observed under a FITC field, and we obtained green fluorescence. The results showed that GPC3-Ab and Ce6-NBs were combined. At the same location, the red fluorescence observed in the red channel indicated successful loading of Ce6 in the GC-NBs (Figure 1E). The absorption spectra of the GC-NBs were similar to the free Ce6 absorption spectra, while the absorption spectra of the NBs showed no obvious absorption peaks. Simultaneously, the maximal absorption peak appeared at a wavelength of 403 nm, and there was no obvious interference of the NBs absorption peak in this band (Figure 2A). These qualitative analysis results indicated that Ce6 with spontaneous red fluorescence was successfully loaded into the NBs. The standard curve of Ce6 derived from the test showed high linearity, accuracy and reproducibility, with a correlation coefficient of 0.9964 (Figure S2), which provided support for obtaining encapsulation efficiency (EE%). The Ce6 encapsulation efficiency (EE%) of the GC-NBs was 71.5% , indicating that the encapsulated Ce6 in the NBs was highly efficient. The successful loading of Ce6 and the successful ligation of GPC3-Ab provided the prerequisites for our targeted sonodynamic strategy.

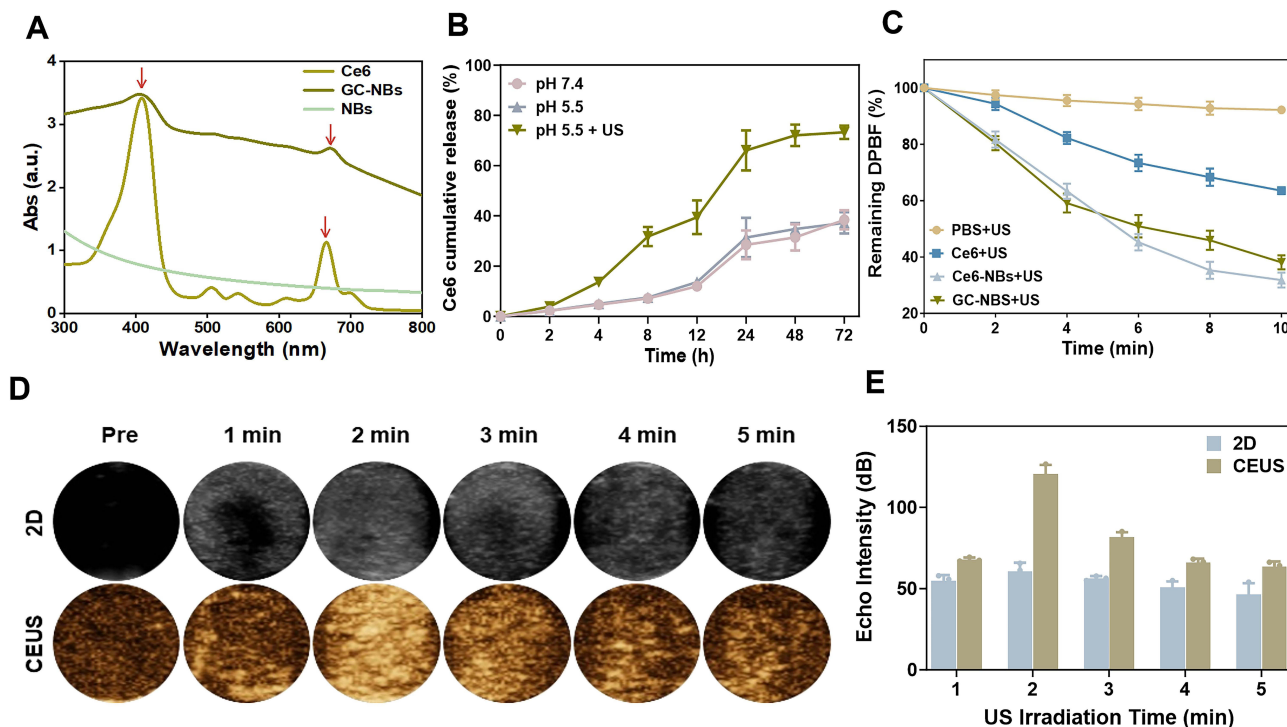


Figure 2 Characterization of GC-NBs.

Notes: (A) Determination of the Ce6 full wavelength absorption spectrum. (B) The drug release from GC-NBs under different conditions. (C) $^1\text{O}_2$ production of the different groups under ultrasound irradiation. (D) Ultrasound imaging of GC-NBs with prolonged ultrasound irradiation time. (E) The corresponding echo intensities of GC-NBs.

In vitro responsive drug release from GC-NBs activated by ultrasound

To investigate drug-releasing behavior under different conditions, three groups were formed, namely, pH 7.4, pH 5.5 and pH 5.5+US. As displayed in Figure 2B, Ce6 was continuously released from the nanobubbles without ultrasound irradiation but burst release of the drug was observed in the nanobubbles after ultrasound exposure. External ultrasound radiation is necessary for the ultrasound-mediated drug delivery.⁴¹ In the pH 7.4 group and pH 5.5 group, no obvious burst drug-releasing profiles were observed because no external stimulus was used and liquid perfluorocarbon kept steady and did not change to the gas phase. Liquid PFP encapsulated in GC-NBs could change to the gas phase in the ultrasound irradiation. Subsequently, nanobubbles were formed and exploded resulting in Ce6 release from the nanodelivery system.

In vitro Singlet Oxygen Generation and Ultrasound Imaging

To confirm ROS generation under ultrasound irradiation, the production of singlet oxygen was investigated in vitro with the aid of an ROS probe (1,3-diphenylisobenzofuran, DPBF).^{42,43} The intensity of the DPBF absorption peak at 415 nm decreased with increasing ultrasound irradiation time because the furan ring in DPBF was destroyed by ROS (Figure S3). In addition, the changes in DPBF absorption at 415 nm under different treatment conditions showed that the loss of DPBF absorption in the probe group mixed with the Ce6-NBs group and the GC-NBs group after ultrasound irradiation was significantly greater than that in the other control groups, indicating that the Ce6-NBs group and the GC-NBs group produced more ¹O₂ after ultrasound irradiation (Figure 2C). The above experiments showed that Ce6-NBs and GC-NBs could increase the level of ROS in the tumour site and could be used to enhance the therapeutic effects of SDT. As shown in Figure 2D and E, an echo signal was not detected for the GC-NBs before ultrasonic irradiation, either in 2D or CEUS mode. With increasing irradiation time, the imaging ability of low-intensity US-induced ADV was related to time. Gradually changing echo signals could be detected in 2D mode and CEUS mode. The strongest echo signal was detected after 2 min at a 2.0 W/cm² intensity and then attenuated quickly. These results demonstrated that the phase change of PFP could be visualized via ultrasonic monitoring during treatment.

Cell Targeting Efficiency

We then tested the cellular uptake of GC-NBs using HepG2 cells with high expression of GPC3. After 6 h of coincubation of Ce6-NBs with cells, no fluorescence was detected in the FITC field, but red fluorescence was detected in the Ce6 field, and only a small amount of red fluorescence was detected around the cells. However, after 6 h of coincubation of FITC-IgG-GC-NBs with cells, fluorescence was clearly visible in both the FITC field and Ce6 field, and the green and red fluorescence around the cells were linked (Figure 3A). These results not only further demonstrated the successful construction of the GPC3-Ab targeted nanodelivery system but also indicated the ability of GC-NBs to target HepG2 cells. Ce6 fluorescence was applied to track the internalization of the nanobubbles via flow cytometry in HepG2 cells. It was not difficult to see from the comparison between the experimental group and the PBS group that Ce6-NBs can enter tumour cells through an endocytosis pathway after coincubation for the same time of 6 h. The cell uptake rate of Ce6-NBs was approximately 26.34%, but the uptake rate of the GC-NB nanodelivery system was approximately 87.19%, which was significantly greater than that of the Ce6-NBs group (Figure 3B). The results showed that the uptake of GC-NBs by tumour cells was closely related to the presence of GPC3-Ab, which successfully identified specific targets on the surface of tumour cells, increased the aggregation of nanobubbles around tumour cells, and improved the delivery efficiency of the nanobubbles.

In vitro Cytotoxicity and Targeted SDT Capability

Considering that sonosensitizers may also exhibit toxicity in the absence of ultrasound irradiation,⁴⁴ we performed hemolysis test for different concentrations of GC-NBs. The hemolytic capacity of GC-NBs to blood was greater than 5% only when the concentration of Ce6 was 8 µg/mL (Figure 3C). We also explored the toxicity of GC-NBs to HUVECs and HepG2 cells by CCK-8 assay. As shown in Figure 3D and E, no obvious cytotoxicity to HUVECs was detected even when the concentration of Ce6 reached 8 µg/mL, indicating the high biosafety of GC-NBs for normal cells. However, when the concentration of Ce6 was greater than 2 µg/mL, significant cytotoxicity to HepG2 cells was detected. Therefore, we used a Ce6 concentration of 2 µg/mL for subsequent experiments. CCK-8 and hemolysis assays revealed

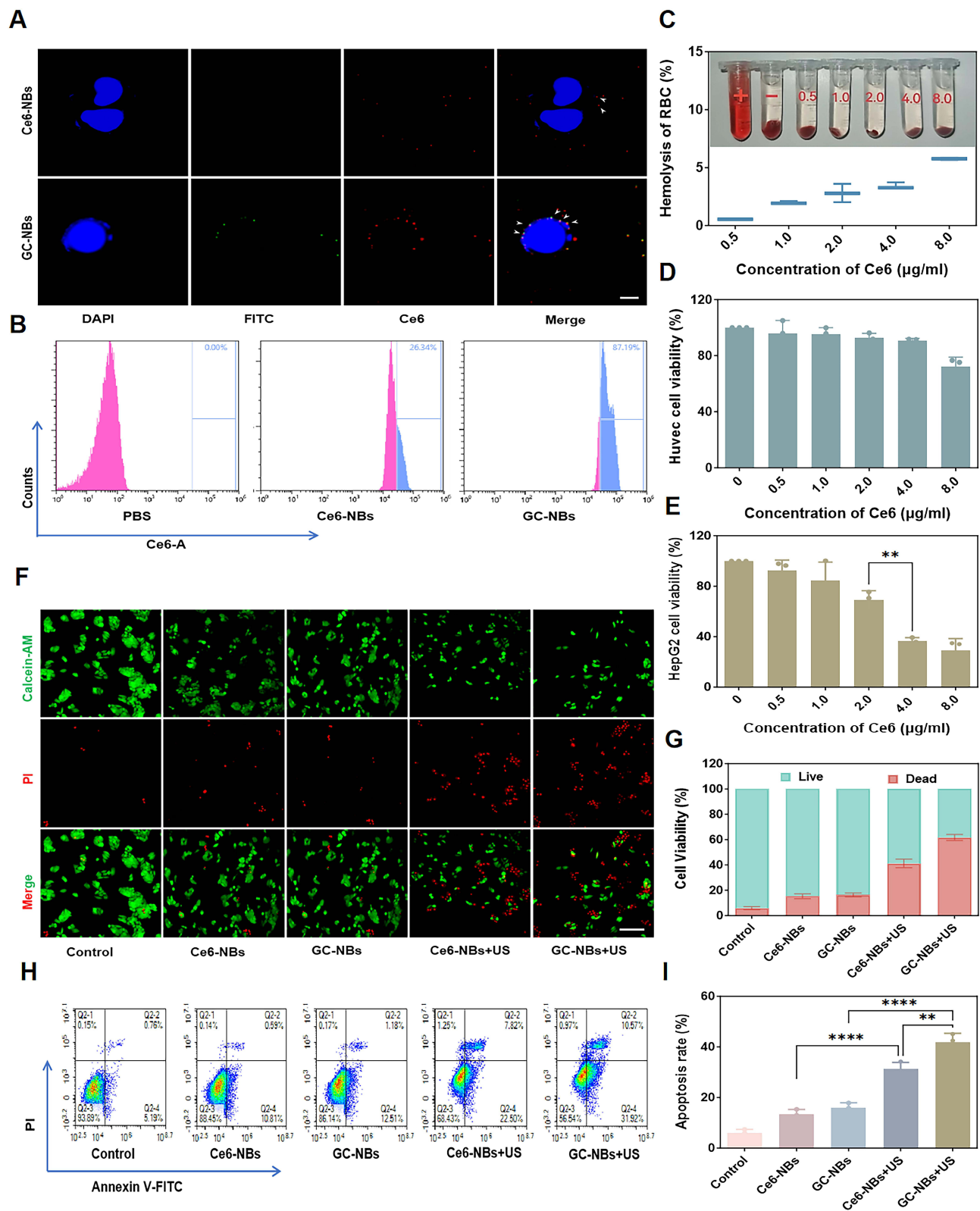


Figure 3 Cellular uptake, Cytotoxicity and SDT of GC-NBs.

Notes: (A) Cellular uptake of GC-NBs in HepG2 cells using fluorescence microscopy. Scale bar: 5 µm. (white arrow mark the Ce6-NBs or GC-NBs on the cell surface). (B) Cellular uptake of GC-NBs in HepG2 cells using flow cytometry. (C) Hemolytic capacity of GC-NBs. (D and E) Relative cell viability of HUVECs and HepG2 cells at different concentrations for 24 h incubation of GC-NBs. (F) Fluorescence images of live/dead cell staining after different treatments. Scale bar: 100 µm. (G) Statistical results of live/dead cell staining in HepG2 cells. (H) The Annexin-V/PI apoptosis assay of HepG2 cells after treated with each group measured by FCM analysis. (I) Statistical results from different experiments of cell apoptosis in HepG2 cells. Data are presented as mean ± SD, n = 3; **p < 0.01, ****p < 0.0001.

that the targeted GC-NBs nanodelivery system had good biocompatibility *in vitro*. Next, we assessed the antitumour ability of GC-NBs *in vitro* (Figure 3F). In the absence of ultrasound irradiation, only a small amount of red fluorescence was observed in the Ce6-NBs group and the GC-NBs group, and strong red fluorescence was evident after ultrasound irradiation. However, the GC-NBs+US group had the strongest red fluorescence. The results of the fluorescence quantitative analysis were consistent with the results of the picture presentation (Figure 3G). There were significantly more dead cells in the GC-NBs+US group than in the Ce6-NBs+US group ($p < 0.001$). The therapeutic effect of targeted SDT was also confirmed by apoptosis assays. The apoptosis of HepG2 cells appeared to follow a trend similar to that of the cell viability results (Figure 3H and I). Compared to the control group, limited apoptosis was observed in HepG2 cells treated with Ce6-NBs and GC-NBs without ultrasound irradiation. This difference could be explained by infinitesimal drug leakage under intrinsic intracellular oxidation conditions in the absence of ultrasound irradiation. Compared with nontargeted Ce6-NBs, the targeted GC-NBs nanodelivery system induced significant apoptosis under ultrasound irradiation ($p < 0.01$). These results indicated that targeted SDT had a remarkable therapeutic effect.

The main strategy of sonodynamic therapy (SDT) is that when exposed to ultrasound, the sonosensitizer is prone to trigger ROS production — a series of single-electron reduction products — to induce cancer cell apoptosis and inhibit cell proliferation.⁴⁵ Herein, we investigated the differences in intracellular ROS among the different groups (Figure 4A). The HepG2 cells from the Ce6-NBs group and GC-NBs group all showed little green fluorescence, but there was no marked difference between these two groups. Strong green fluorescence was observed in the Ce6-NBs+US group and GC-NBs+US group. Surprisingly, the intracellular green fluorescence intensity was the strongest in the GC-NBs+US group. The results of the quantitative analysis of fluorescence intensity were consistent with the images (Figure 4B), which demonstrated that the targeting effect of GPC3-Ab promoted the aggregation of Ce6-NBs in HepG2 cells, thereby increasing the production of ROS. We then assessed changes in the mitochondrial membrane potential ($\Delta\Psi_m$) of HepG2 cells. As shown in Figure 4C, the cells in the Ce6-NBs group and GC-NBs group exhibited intense red fluorescence, similar to that of the control group, while the cells in the Ce6-NBs+US group exhibited green fluorescence. In addition, the presence of the GC-NBs under ultrasound irradiation further increased the green fluorescence intensity of the HepG2 cells, indicating a significant decrease in the $\Delta\Psi_m$. Fluorescence intensity quantification analysis of the monomer/aggregate ratio showed consistent results (Figure 4D). After HepG2 cells in the GC-NBs+US group were treated, the JC-1 aggregates within the mitochondria converted to a monomeric form and significantly increased the monomer/aggregate ratio. These data illustrated that the nanodelivery system GC-NBs could significantly induce changes in the mitochondrial membrane potential under ultrasound irradiation, which in turn led to the apoptosis of tumour cells.

In vivo Targeting Capability and Biodistribution

Considering that active targeting *in vivo* is mediated by GPC3-Ab, the fluorescence characteristics of Ce6 were used to further explore the targeting capability and biodistribution of GC-NBs *in vivo*. As depicted in Figure 5A, the tumour regions exhibited different degrees of fluorescence signal at 1–24 h postinjection, and the fluorescence signal peaked at 3 h postadministration in the GC-NBs group. Comparatively, there was a relatively weak fluorescence signal in the tumour after the injection of Ce6-NBs, suggesting that some nanobubbles accumulated in the tumour via the EPR effect. By observing the fluorescence signal of Ce6 in the tumour tissue 48 hours after injection, it was shown that more GC-NBs could be retained in the tumour tissue (Figure 5B and C). To further observe the biodistribution of the fabricated GC-NBs, the major tissues were harvested for fluorescence imaging (Figure S4). The images revealed that GC-NBs mainly accumulated in the liver as a result of phagocytosis by the reticuloendothelial system. These results demonstrated the efficient accumulation of GC-NBs in the tumour under the guidance of the GPC3-Ab targeting effect, which plays an important role in further tumoral distribution.

In vivo Targeted SDT Evaluation

With previous exciting results showing enhanced nanobubbles accumulation in tumours through active targeting of GPC3-Ab, the anticancer efficacy of GC-NBs *in vivo* was evaluated in H22 xenograft mouse model (Figure 6A). The tumour volume and tumour weight data showed that tumour growth was inhibited by Ce6-NBs or GC-NBs alone but was still relatively fast, indicating that Ce6-NBs or GC-NBs alone had a limited effect on tumours. In the Ce6-NBs+US group

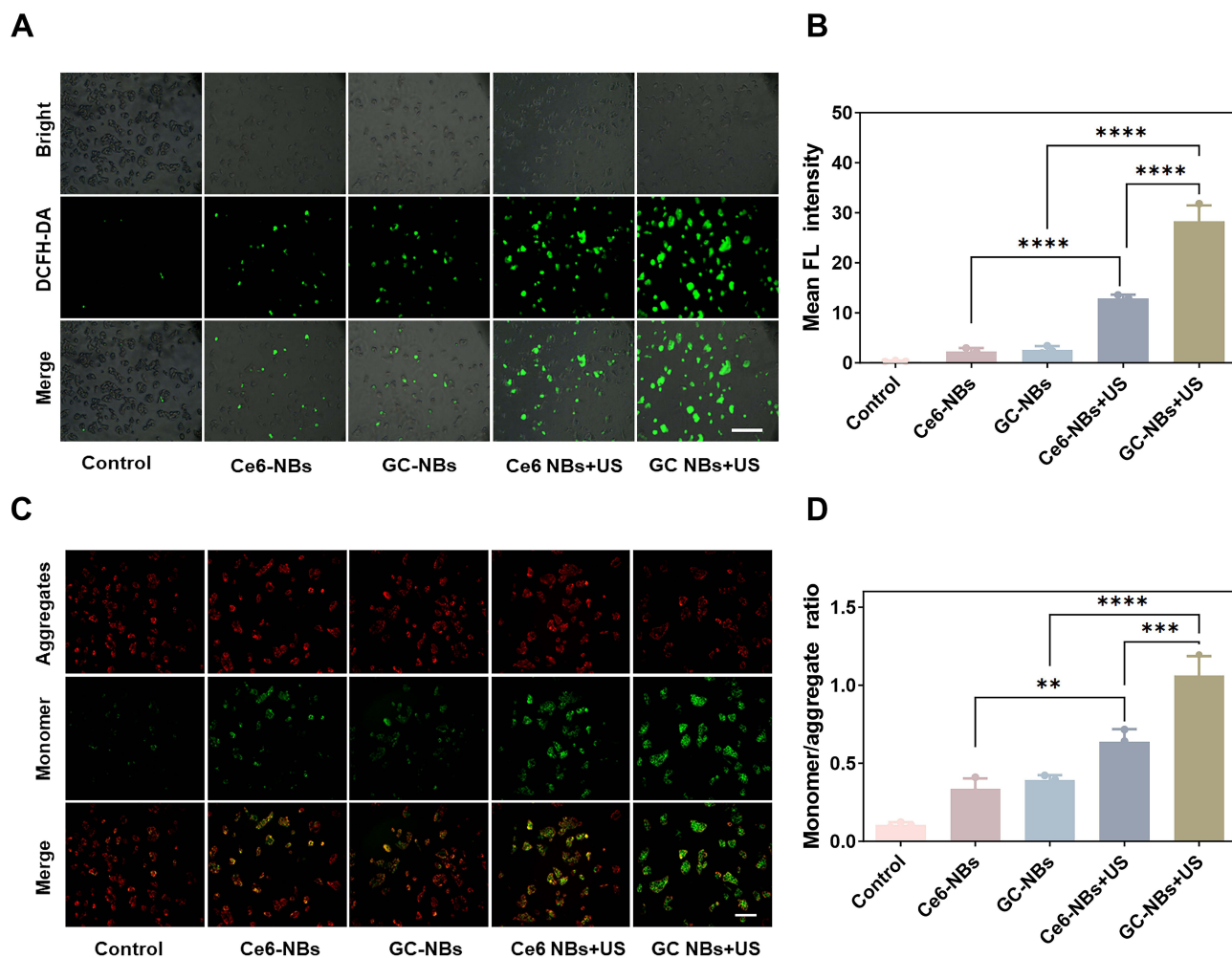


Figure 4 Detection of intracellular ROS generation and mitochondrial membrane depolarization.

Notes: (A) Production of ROS in HepG2 cells of different groups under fluorescence microscopy. Scale bar: 100 μ m. (B) The quantification of fluorescence intensity in different groups. (C) Fluorescence microscopic imaging of HepG2 cells stained with JC-1 under different treatments. Scale bar: 50 μ m. (D) The aggregate/monomer fluorescence intensity ratio of JC-1. Data are presented as mean \pm SD, n = 3; **P < 0.01, ***P < 0.001, ****P < 0.0001.

and the GC-NBs+US group, the tumour growth rate further decreased, and the inhibitory effect was more pronounced than that of Ce6-NBs or GC-NBs alone. Notably, the tumour suppressive effect was more pronounced in the GC-NBs+US group than in the Ce6-NBs+US group (Figure 6B and C). The volume inhibition rate and weight inhibition rate of the GC-NBs+US group were $73.46 \pm 2.53\%$ and $81.78 \pm 4.5\%$, respectively (Figure S5). The morphological characteristics of the tumours after treatment were also consistent with the above results (Figure 6D), and the therapeutic effect in the GC-NBs+US group was significantly greater than that in the other groups, suggesting that our targeted sonodynamic strategy was viable. Unfortunately, our targeted sonodynamic strategy cannot completely eliminate tumours; this might be due to the following reasons. The singlet oxygen generated by Ce6 under the action of ultrasound is easily consumed by the high content of glutathione (GSH) in the tumour microenvironment, so an insufficient therapeutic effect is obtained.⁴⁶ Hematoxylin/eosin (HE), TdT-dependent dUTP-biotin nick end labeling (TUNEL), and proliferating cell nuclear antigen (Ki-67) staining of tumour sections further verified the anticancer efficacy of the different treatments (Figure 6E). HE staining revealed greater necrosis of tumour cells in the GC-NBs+US group than in the other groups. The results of the TUNEL assay showed that a large number of apoptotic cells were found in the GC-NBs+US group. The results of Ki-67 staining also suggested that GC-NBs+US significantly inhibited tumour cell proliferation. Therefore, the above results demonstrated that GC-NBs+US effectively improved the therapeutic effect on hepatocellular carcinoma.

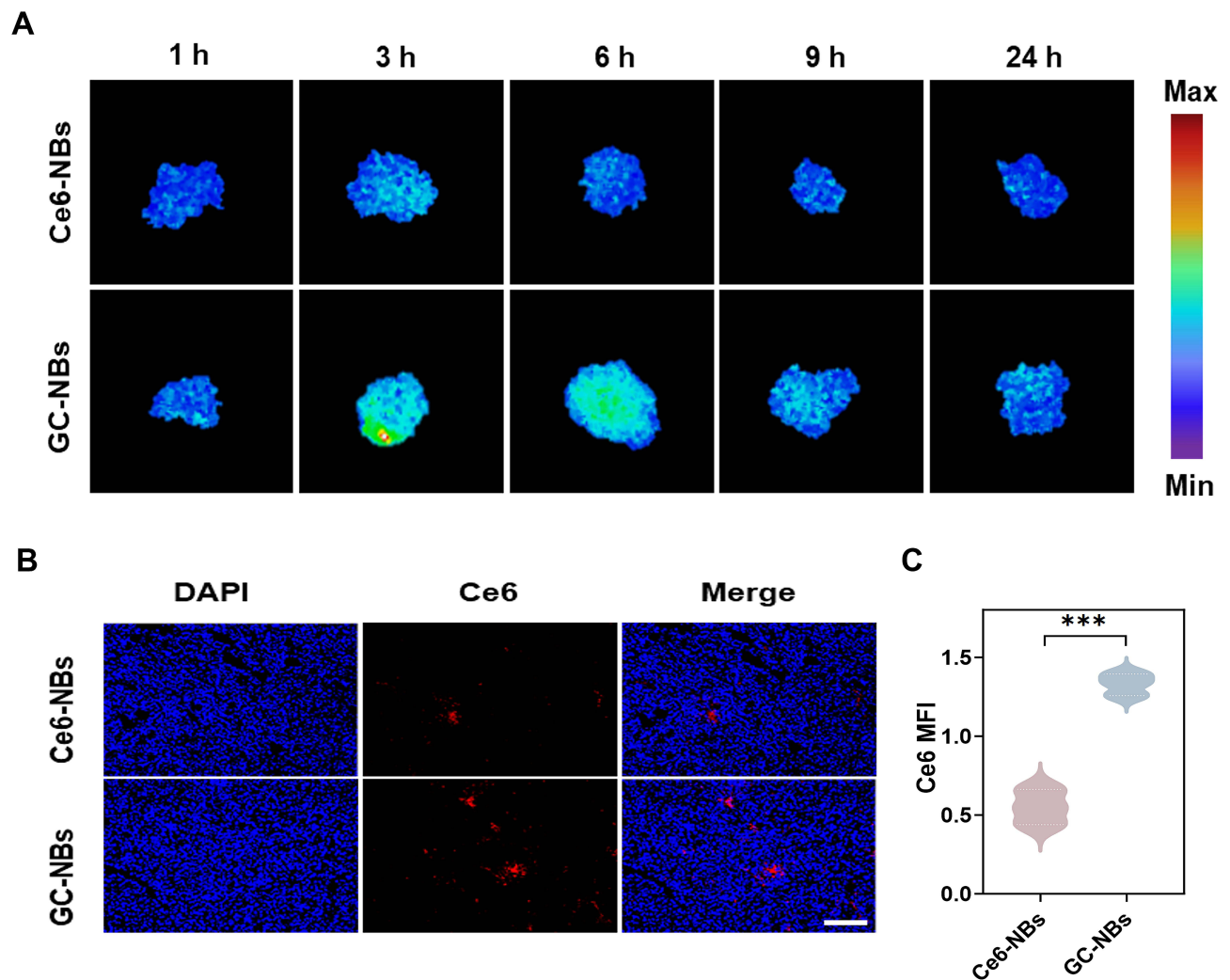


Figure 5 Targeting capability of GC-NBs in vivo.

Notes: (A) Fluorescence imaging of the tumors at 1 h, 3 h, 6 h, 9 h and 24 h post-injection. (B) Fluorescence intensity of Ce6 in the tissue at 48 h post-injection. Scale bar: 100 μ m. (C) Quantitative analysis of the fluorescence intensity of Ce6 shown in panel. Data are presented as mean \pm SD, n = 3; *** P <0.001.

In vivo Ultrasound Imaging

Considering the in vitro Ultrasound imaging performance of GC-NBs, we next validated the in vivo imaging performance of GC-NBs. First, the GC-NBs solution was intravenously injected into tumour-bearing mice. Ultrasound irradiation was administered 3 h after the peak accumulation time at the tumour site. Then, Ultrasound imaging system was used to acquire enhanced Ultrasound images of the tumour masses. Upon Ultrasound stimulation, the tumour regions were highlighted with a large Ultrasound echo signal after the injection of the GC-NBs. The echo intensity within the tumour areas was also greater after the injection than before the injection (Figure 5D and E). The results inspired us to apply this nanodelivery system to visualize hepatocellular carcinoma therapy.

In vivo safety evaluation

Biosafety of nanodelivery system was one of the necessary conditions for its application in vivo, so this factor of GC-NBs was evaluated in vivo. Liver damage in the mice in each group was evaluated after treatment, alanine aminotransferase (ALT) and aspartate aminotransferase (AST) were used as liver function indicators, and there was no significant difference in the ALT and AST levels in the mice in each group compared with those in the control group

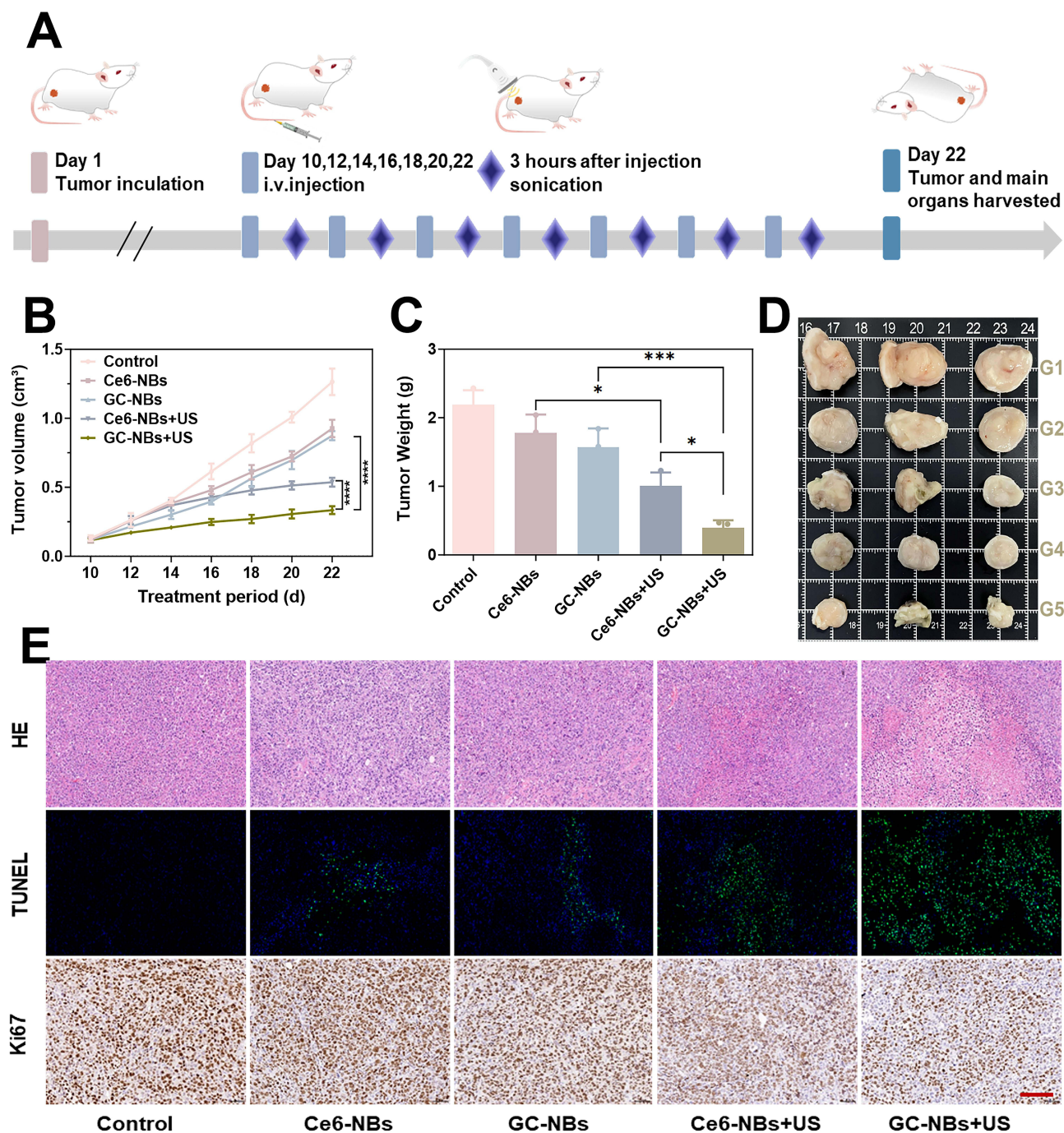


Figure 6 In vivo anti-cancer properties.

Notes: (A) In vivo experimental treatment plan. (B) Tumor growth curve of each group. (C) Tumor weights after different treatments. Data are presented as mean \pm SD, $n = 3$; * $P < 0.05$, *** $P < 0.001$. (D) Photos of tumors. (G1: Control, G2: Ce6-NBs, G3: GC-NBs, G4: Ce6-NBs+US, G5: GC-NBs+US). (E) Immunofluorescence staining micrograph of tumor slices collected from different treatment groups. Scale bar: 100 μ m.

(Figure S6). The organ index was evaluated as a sensitive indicator of organs. There were no significant differences in the organ indices of the heart, liver, spleen, lung or kidney between the treatment groups and the control group (Figure S7). No significant changes were detected in the body weights of the mice in each group, and no pathological changes were detected via HE staining of major organs (Figure 7 and S8). These results indicated that our treatment strategy has a high degree of biosafety.

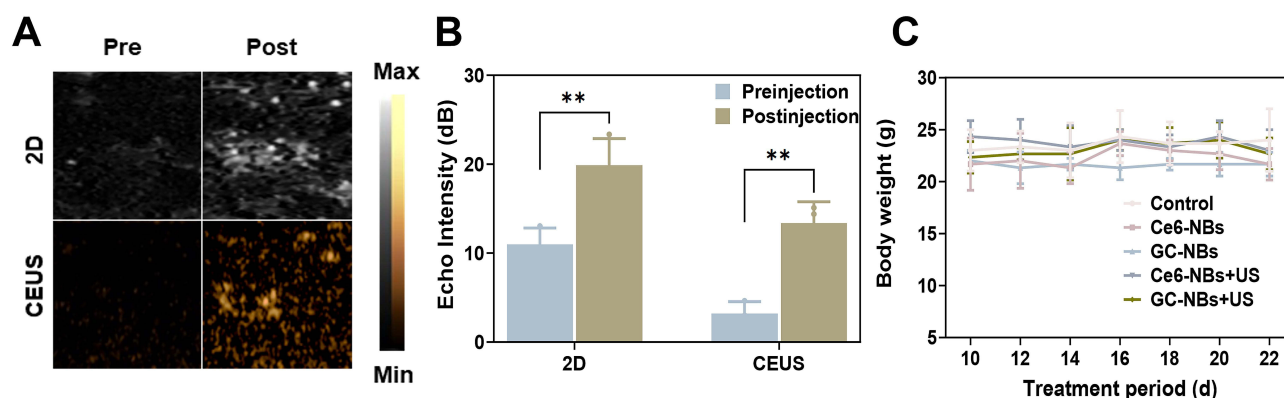


Figure 7 Ultrasound imaging of GC-NBs and safety evaluation in vivo.

Notes: (A) In vivo ultrasound imaging before and after the injection of GC-NBs assisted by ultrasound irradiation. (B) The corresponding quantitative analysis of ultrasound imaging. (C) Body weight of mice during treatment. Data are presented as mean \pm SD, $n = 3$; ** $P < 0.01$.

Conclusion

Herein, we developed a new treatment strategy for more effective antitumour efficacy. In this work, a nanodelivery system was successfully built for combining HCC-specific targeting and stimuli-responsive controlled release to simultaneously integrate targeted therapy with visualized SDT. The nanodelivery system exhibited high Ce6 encapsulation, a good ability to target HepG2 cells, and enhanced ultrasound imaging, leading to potent antitumour growth in vivo. Last but not the least, the whole system is safe and stable with excellent biocompatibility. This study therefore provides a proof-of-concept demonstration of visualized targeted sonodynamic therapy for HCC, and we expect this strategy to be broadly applicable to other cancer types.

Abbreviations

DPPC, 1,2-dipalmitoyl-sn-glycerol-3-phosphatidylcholine; DPPE-mPEG2000, 1,2-dipalmitoyl-sn-glycerol-3-phospholipid ethanolamine-polyethylene glycol-2000; Ce6, chlorine e6; PFP, perfluoropentane; GPC3-Ab, glypican-3-antibody; DMEM, high glucose dulbecco's modified eagle medium; FBS, fetal bovine serum; EDTA, ethylenediaminetetraacetic acid; DLS, dynamic light scattering; TEM, transmission electron microscopy; EE, encapsulation efficiency; DPBF, 1,3-diphenyl isobenzofuran; DCFH-DA, 2,7-dichlorofluorescein diacetate; US, ultrasound; CEUS, contrast enhance ultrasound; HE, hematoxylin /eosin; TUNEL, TdT-dependent dUTP-biotin nick end labeling; Ki-67, proliferating cell nuclear antigen.

Funding

This study was financially supported by the fund of the Bureau of Science and Technology and Intellectual Property Nanchong city (Grant No: 22SXQT0302), the Bureau of Science and Technology and Intellectual Property Nanchong city (Grant No: 22SXQT0294), the affiliated hospital of north Sichuan medical college (Grant No. 2021LC009) and the opening project of medical imaging key laboratory of Sichuan province (Grant No. MIKLSP2021010).

Disclosure

The authors report no conflicts of interest in this work.

References

- Vogel A, Meyer T, Sapisochin G, Salem R, Saborowski A. Hepatocellular carcinoma. *Lancet*. 2022;400(10360):1345–1362. doi:10.1016/s0140-6736(22)01200-4
- Sung H, Ferlay J, Siegel RL, et al. global cancer statistics 2020: globocan estimates of incidence and mortality worldwide for 36 Cancers in 185 Countries. *CA Cancer J Clin*. 2021;71(3):209–249. doi:10.3322/caac.21660
- Siegel RL, Miller KD, Wagie NS, Jemal A. Cancer statistics, 2023. *CA Cancer J Clin*. 2023;73(1):17–48. doi:10.3322/caac.21763

4. Maluccio M, Covey A. Recent progress in understanding, diagnosing, and treating hepatocellular carcinoma. *CA Cancer J Clin.* 2012;62(6):394–399. doi:10.3322/caac.21161
5. Yang JD, Heimbach JK. New advances in the diagnosis and management of hepatocellular carcinoma. *BMJ.* 371;<pg>m3544. doi:10.1136/bmj.m3544
6. Forner A, Reig M, Bruix J. Hepatocellular carcinoma. *Lancet.* 2018;391(10127):1301–1314. doi:10.1016/s0140-6736(18)30010-2
7. Yang B, Chen Y, Shi J. Reactive Oxygen Species (ROS)-Based Nanomedicine. *Chem Rev.* 2019;119(8):4881–4985. doi:10.1021/acs.chemrev.8b00626
8. Cheung EC, Vousden KH. The role of ROS in tumour development and progression. *Nat Rev Cancer.* 2022;22(5):280–297. doi:10.1038/s41568-021-00435-0
9. Nakamura H, Takada K. Reactive oxygen species in cancer: current findings and future directions. *Can Sci.* 2021;112(10):3945–3952. doi:10.1111/cas.15068
10. Liang S, Deng X, Ma P, Cheng Z, Lin J. Recent advances in nanomaterial-assisted combinational sonodynamic cancer therapy. *Adv Mater.* 2020;32(47):e2003214. doi:10.1002/adma.202003214
11. Beguin E, Shrivastava S, Dezhkunov NV, McHale AP, Callan JF, Stride E. direct evidence of multibubble sonoluminescence using therapeutic ultrasound and microbubbles. *ACS Appl Mater Interfac.* 2019;11(22):19913–19919. doi:10.1021/acsami.9b07084
12. Gong Z, Dai Z. Design and challenges of sonodynamic therapy system for cancer theranostics: from equipment to sensitizers. *Adv Sci.* 2021;8(10):2002178. doi:10.1002/advs.202002178
13. Huang J, Liu F, Han X, et al. Nanosensitizers for highly efficient sonodynamic cancer theranostics. *Theranostics.* 2018;8(22):6178–6194. doi:10.7150/thno.29569
14. Liao S, Cai M, Zhu R, et al. Antitumor Effect of photodynamic therapy/sonodynamic therapy/sono-photodynamic therapy of chlorin e6 and other applications. *Mol Pharm.* 20(2):875–885. doi:10.1021/acs.molpharmaceut.2c00824
15. Jiang Q, Qiao B, Lin X, et al. A hydrogen peroxide economizer for on-demand oxygen production-assisted robust sonodynamic immunotherapy. *Theranostics.* 2022;12(1):59–75. doi:10.7150/thno.64862
16. Dymek M, Sikora E. Liposomes as biocompatible and smart delivery systems – the current state. *Adv Colloid Interface Sci.* 2022;309. doi:10.1016/j.cis.2022.102757
17. Meng Z, Zhang Y, Shen E, et al. Marriage of virus-mimic surface topology and microbubble-assisted ultrasound for enhanced intratumor accumulation and improved cancer theranostics. *Adv Sci.* 2021;8(13).
18. Mossenta M, Busato D, Dal Bo M, Macor P, Toffoli G. Novel nanotechnology approaches to overcome drug resistance in the treatment of hepatocellular carcinoma: glypican 3 as a useful target for innovative therapies. *Int J Mol Sci.* 2022;23(17):10038.
19. Li D, Li N, Zhang Y-F, et al. Persistent polyfunctional chimeric antigen receptor T Cells that target glypican 3 eliminate orthotopic hepatocellular carcinomas in mice. *Gastroenterology.* 2020;158(8):2250–2265.e20. doi:10.1053/j.gastro.2020.02.011
20. Deng H, Shang W, Wang K, et al. Targeted-detection and sequential-treatment of small hepatocellular carcinoma in the complex liver environment by GPC-3-targeted nanoparticles. *J Nanobiotechnol.* 2022;20(1):156.
21. Feng K, Li X, Huang A, Wan M, Zong Y. Effect of tissue viscoelasticity and adjacent phase-changed microbubbles on vaporization process and direct growth threshold of nanodroplet in an ultrasonic field. *Ultrason Sonochem.* 2023;101:106665.
22. Namen AV, Jandhyala S, Jordan T, Luke GP. Repeated acoustic vaporization of perfluorohexane nanodroplets for contrast-enhanced ultrasound imaging. *IEEE Trans Ultrason Ferroelectr Freq Control.* 2021;68(12):3497–3506. doi:10.1109/tuffc.2021.3093828
23. Fan K, Zeng L, Guo J, et al. Visualized podocyte-targeting and focused ultrasound responsive glucocorticoid nano-delivery system against immune-associated nephropathy without glucocorticoid side effect. *Theranostics.* 2021;11(6):2670–2690. doi:10.7150/thno.53083
24. Gao X, Guo D, Mao X, Shan X, He X, Yu C. Perfluoropentane-filled chitosan poly-acrylic acid nanobubbles with high stability for long-term ultrasound imaging in vivo. *Nanoscale.* 2021;13(10):5333–5343. doi:10.1039/d0nr06878k
25. Chen K-W, Hsu P-H, Huang H-L, et al. Targeting nanoparticle-conjugated microbubbles combined with ultrasound-mediated microbubble destruction for enhanced tumor therapy. *Pharmacol Res.* 2022;186. doi:10.1016/j.phrs.2022.106532
26. Wang J, Zhang W, Xie Z, et al. Magnetic nanodroplets for enhanced deep penetration of solid tumors and simultaneous magnetothermal-sensitized immunotherapy against tumor proliferation and metastasis. *Adv Healthcare Mater.* 2022;11(23). doi:10.1002/adhm.202201399
27. Xi L, Han Y, Liu C, et al. Sonodynamic therapy by phase-transition nanodroplets for reducing epidermal hyperplasia in psoriasis. *J Control Release.* 2022;350:435–447. doi:10.1016/j.jconrel.2022.08.038
28. Li J, Ji H, Jing Y, Wang S. pH- and acoustic-responsive platforms based on perfluoropentane-loaded protein nanoparticles for ovarian tumor-targeted ultrasound imaging and therapy. *Nanoscale Res Lett.* 15(1):31. doi:10.1186/s11671-020-3252-z
29. Wang G, Jiang Y, Xu J, et al. Unraveling the Plasma Protein Corona by Ultrasonic Cavitation Augments Active-Transporting of Liposome in Solid Tumor. *Adv Mater.* 2023;35(9):e2207271. doi:10.1002/adma.202207271
30. Yang Y, Zhang JY, Ma ZJ, et al. Visualization of therapeutic intervention for acute liver injury using low-intensity pulsed ultrasound-responsive phase variant nanoparticles. *Biomater Sci.* 2024. doi:10.1039/d3bm01423a
31. Mu W, Jiang D, Mu S, Liang S, Liu Y, Zhang N. Promoting early diagnosis and precise therapy of hepatocellular carcinoma by glypican-3-targeted synergistic chemo-photothermal theranostics. *ACS Appl Mater Interfac.* 2019;11(26):23591–23604. doi:10.1021/acsami.9b05526
32. Briuglia M-L, Rotella C, McFarlane A, Lamprou DA. Influence of cholesterol on liposome stability and on in vitro drug release. *Drug Del Transl Res.* 2015;5(3):231–242. doi:10.1007/s13346-015-0220-8
33. Li Y, Zhang X, Cao D. Nanoparticle hardness controls the internalization pathway for drug delivery. *Nanoscale.* 2015;7(6):2758–2769. doi:10.1039/c4nr05575f
34. Liu Y, Yang S, Zhou Q, et al. Nanobubble-based anti-hepatocellular carcinoma therapy combining immune check inhibitors and sonodynamic therapy. *Nanoscale Adv.* 4(22):4847–4862. doi:10.1039/d2na00322h
35. Perry JL, Reuter KG, Luft JC, Pecot CV, Zamboni W, DeSimone JM. Mediating Passive Tumor Accumulation through Particle Size, Tumor Type, and Location. *Nano Lett.* 2017;17(5):2879–2886.
36. Pashizeh F, Mansouri A, Bazzazan S, et al. Bioresponsive gingerol-loaded alginate-coated niosomal nanoparticles for targeting intracellular bacteria and cancer cells. *Int J Biol Macromol.* 2024;258d7. doi:10.1016/j.ijbiomac.2023.128957

37. Dastneshan A, Rahiminezhad S, Naderi Mezajin M, et al. Cefazolin encapsulated UIO-66-NH₂ nanoparticles enhance the antibacterial activity and biofilm inhibition against drug-resistant *S. aureus*: in vitro and in vivo studies. *Chem Eng J.* 2023;455. doi:10.1016/j.cej.2022.140544
38. Hu S, Xia K, Huang X, et al. Multifunctional CaCO₃@Cur@QTX125@HA nanoparticles for effectively inhibiting growth of colorectal cancer cells. *J Nanobiotech.* 2023;21(1).
39. Dwivedi P, Kiran S, Han S, et al. Magnetic Targeting and Ultrasound Activation of Liposome–Microbubble Conjugate for Enhanced Delivery of Anticancer Therapies. *ACS Appl Mater Interfac.* 2020;12(21):23737–23751. doi:10.1021/acsami.0c05308
40. Chen Y, Luo X, Liu Y, et al. Targeted Nanobubbles of PD-L1 mAb Combined with Doxorubicin as a Synergistic Tumor Repressor in Hepatocarcinoma. *Int J Nanomed.* 2022;17:3989–4008. doi:10.2147/ijn.S376172
41. Cao Y, Chen Y, Yu T, et al. Drug Release from Phase-Changeable Nanodroplets Triggered by Low-Intensity Focused Ultrasound. *Theranostics.* 2018;8(5):1327–1339. doi:10.7150/thno.21492
42. Yu L, Wang Z, Mo Z, et al. Synergetic delivery of triptolide and Ce6 with light-activatable liposomes for efficient hepatocellular carcinoma therapy. *Acta Pharmaceutica Sinica B.* 2021;11(7):2004–2015. doi:10.1016/j.apsb.2021.02.001
43. Zamojć K, Zdrowowicz M, Rudnicki-Velasquez PB, et al. The development of 1,3-diphenylisobenzofuran as a highly selective probe for the detection and quantitative determination of hydrogen peroxide. *Free Radic Res.* 2016;51(1):38–46. doi:10.1080/10715762.2016.1262541
44. Jin Y, Zhou Q, Geng J, et al. Sonodynamic effects of a novel ether-group modified porphyrin derivative combined with pulsed low-intensity ultrasound on PC-9 Cells. *Front Pharmacol.* 2021;12. doi:10.3389/fphar.2021.792360
45. Lin X, Song J, Chen X, Yang H. Ultrasound-activated sensitizers and applications. *Angew Chem Int Ed.* 2020;59(34):14212–14233. doi:10.1002/anie.201906823
46. Kiesslich T, Plaetzer K, Oberdanner CB, Berlanda J, Obermair FJ, Krammer B. Differential effects of glucose deprivation on the cellular sensitivity towards photodynamic treatment-based production of reactive oxygen species and apoptosis-induction. *FEBS Lett.* 2004;579(1):185–190. doi:10.1016/j.febslet.2004.11.073

International Journal of Nanomedicine

Dovepress

Publish your work in this journal

The International Journal of Nanomedicine is an international, peer-reviewed journal focusing on the application of nanotechnology in diagnostics, therapeutics, and drug delivery systems throughout the biomedical field. This journal is indexed on PubMed Central, MedLine, CAS, SciSearch[®], Current Contents[®]/Clinical Medicine, Journal Citation Reports/Science Edition, EMBase, Scopus and the Elsevier Bibliographic databases. The manuscript management system is completely online and includes a very quick and fair peer-review system, which is all easy to use. Visit <http://www.dovepress.com/testimonials.php> to read real quotes from published authors.

Submit your manuscript here: <https://www.dovepress.com/international-journal-of-nanomedicine-journal>